Detection and Quantification of Line and Sheet Structures in 3-D Images

Yoshinobu Sato and Shinichi Tamura

Division of Functional Diagnostic Imaging
Osaka University Graduate School of Medicine
Room D11, 2-2 Yamada-Oka, Suita, Osaka, 565-0871, Japan
yoshi@image.med.osaka-u.ac.jp,
http://www.image.med.osaka-u.ac.jp/∼yoshi

Abstract. This paper describes a method for the accurate segmentation of line and sheet structures in 3-D images with the aim of quantitatively evaluating anatomical structures in medical images with line-like shapes such as blood vessels and sheet-like shapes such as articular cartilages. Explicit 3-D line and sheet models are utilized. The line model is characterized by medial axes associated with variable cross-sections, and the sheet model by medial surfaces with spatially variable widths. The method unifies segmentation, model recovery, and quantification to obtain 3-D line and sheet models by fully utilizing formal analyses of 3-D local intensity structures. The local shapes of these structures are recovered and quantitated with subvoxel resolution using spatially variable directional derivatives based on moving frames determined by the extracted medial axes and surfaces. The medial axis detection performance and accuracy limits of the quantification are evaluated using synthesized images. The clinical utility of the method is demonstrated through experiments in bronchial airway diameter estimation from 3-D computed tomography (CT) and cartilage thickness determination from magnetic resonance (MR) images.

1 Introduction

With high-resolution 3-D imaging modalities becoming commonly available in medical imaging, a strong need has arisen for a means of accurately quantifying in 3-D anatomical structures of interest from acquired 3-D images. In the 2-D domain, the quantification of vessel diameters from 2-D X-ray projective images has been intensively studied [1],[2] in both the diagnostic imaging and image analysis research communities. As a result, image analysis for 2-D vessel diameter estimation is now recognized as an essential tool for accurate and objective diagnosis. Nevertheless, serious limitations to 2-D quantification as projections of 3-D objects have been pointed out [3]. The goal of this paper is to develop a well-formulated method for such quantification in the 3-D domain.

From the viewpoint of image analysis, the quantification of vessel diameters in 2-D is regarded as the recovery of segmented line descriptions, which typically

S.L. Delp, A.M. DiGioia, and B. Jaramaz (Eds.): MICCAI 2000, LNCS 1935, pp. 154–165, 2000.

consist of the medial axes of lines and the width associated with each point on these axes [4]. The 2-D line is naturally extended to two types of 3-D features: line and sheet [5]. The 3-D line model consists of the *medial axes* of lines [6] and the *cross-sectional shape* associated with each point on these axes, while the 3-D sheet model consists of the *medial surfaces* of sheets and the *width* associated with each point on these surfaces. Examples of line-like structures are ductal structures such as blood vessels and bronchial airways, while structures such as cortices and articular cartilages are regarded as sheet-like.

In this paper, we address the problem of detecting and quantitating line and sheet structures from 3-D images. There has been a considerable amount of work on the detection and description of these structures, which can be categorized into two different approaches, although in general less attention has been paid to sheet-like structures. One approach is to use line and sheet enhancement filtering [5],[7],[8],[9]. Multiscale analysis of 3-D local intensity structures using the eigenvalues of the Hessian matrix has been shown to be effective in discriminating them from other structures as well as in the detection of small structures. However, consideration of 3-D quantification remains insufficient. The other approach is to employ generalized cylinder (GC) recovery [10],[11]. Recovered GCs have rich quantitative parameters, and GC recovery is often applied to successfully extracted contours or surfaces. Nevertheless, the recovery of GCs with arbitrary axes and cross-section is a difficult task, which means that severe restrictions are often imposed on their shapes or user interaction is needed. Unlike these previous approaches, our method unifies segmentation, model recovery, and quantification. While motivated by the GC concept, the method fully utilizes 3-D local intensity structure analysis to obtain explicit 3-D line and sheet models.

The organization of this paper is as follows. In Section 2, we formulate the method for the recovery of line and sheet models, and describe each procedure in detail. In Section 3, we evaluate the basic characteristics and accuracy of the method using synthesized 3-D images, and describe experiments using clinical 3-D data acquired by computed tomography (CT) and magnetic resonance imaging (MRI). Finally, in Section 4 we summarize our conclusions and indicate the directions of future work.

2 Recovery of 3-D Line and Sheet Models

The method is based on a second-order analysis of 3-D local intensity structures. The following is an overview of the method.

Step 1: Existing filtering techniques for line and sheet enhancement are used to extract the initial regions, which should include all potential medial axes and surfaces [7],[9]. These are then used as initial values for the subsequent subvoxel edge localization. The candidate regions, which should include all potential line and sheet regions, are also extracted.

Step 2: The medial axes and surfaces are extracted using local second-order approximation given by the gradient vector and Hessian matrix. The eigenvec-

tors of the Hessian matrix define the moving frames on medial axes/surfaces. After this, the moving frames are embedded in a 3-D image such that each point within the candidate regions is directly related to its corresponding moving frame.

Step 3: Subvoxel edge localization of the region boundaries is carried out using adaptive 3-D directional derivatives, whose directions are adaptively changed depending on the moving frame, to accomplish accurate segmentation, model recovery, and quantification.

In the following, we begin with a description of Step 2 of the method since Step 1 is described in detail in [7] and [9].

2.1 Detection and Subvoxel Localization of Medial Axes and Surfaces

Let $I(\mathbf{x})$ be a 3-D image in which $\mathbf{x} = (x, y, z)^\top$, and $\nabla^2 I(\mathbf{x}; \sigma)$ be the Hessian matrix of the image blurred by the isotropic Gaussian function with a standard deviation σ, which is given by

$$\nabla^2 I(\mathbf{x}; \sigma) = \begin{bmatrix} I_{xx}(\mathbf{x}; \sigma) & I_{xy}(\mathbf{x}; \sigma) & I_{xz}(\mathbf{x}; \sigma) \\ I_{yx}(\mathbf{x}; \sigma) & I_{yy}(\mathbf{x}; \sigma) & I_{yz}(\mathbf{x}; \sigma) \\ I_{zx}(\mathbf{x}; \sigma) & I_{zy}(\mathbf{x}; \sigma) & I_{zz}(\mathbf{x}; \sigma) \end{bmatrix}, \tag{1}$$

where partial second derivatives of the Gaussian blurred image $I(\mathbf{x}; \sigma)$ are represented by expressions like $I_{xx}(\mathbf{x}; \sigma) = \frac{\partial^2}{\partial x^2} I(\mathbf{x}; \sigma)$, $I_{yz}(\mathbf{x}; \sigma) = \frac{\partial^2}{\partial y \partial z} I(\mathbf{x}; \sigma)$, and so on.

The second-order approximation of $I(\mathbf{x}; \sigma)$ around $\mathbf{x}_0$ is given by

$$I_{\mathrm{II}}(\mathbf{x}; \sigma) = I(\mathbf{x}_0; \sigma) + (\mathbf{x} - \mathbf{x}_0)^\top \nabla I_0 + \frac{1}{2}(\mathbf{x} - \mathbf{x}_0)^\top \nabla^2 I_0 (\mathbf{x} - \mathbf{x}_0), \tag{2}$$

where ∇I_0 and $\nabla^2 I_0$ denote the gradient vector and the Hessian matrix combined with the Gaussian blurrring σ at $\mathbf{x}_0$, respectively. Let the eigenvalues of $\nabla^2 I$ be λ_1, λ_2, λ_3 ($\lambda_1 \geq \lambda_2 \geq \lambda_3$) and their corresponding eigenvectors be $\mathbf{e}_1$, $\mathbf{e}_2$, $\mathbf{e}_3$ ($|\mathbf{e}_1| = |\mathbf{e}_2| = |\mathbf{e}_3| = 1$), respectively. Three types of local structures — line, sheet, and blob — can be classified using these eigenvalues [9]. For the ideal line, $\mathbf{e}_1$ is expected to give its tangential direction and both $|\lambda_2|$ and $|\lambda_3|$, directional second derivatives orthogonal to $\mathbf{e}_1$, should be large on its medial axis, while $\mathbf{e}_3$ is expected to give the orthogonal direction of a sheet and only $|\lambda_3|$ should be large on its medial surface (Fig. 1). Here, structures of interest are assumed to be brighter than surrounding regions.

The initial regions obtained in Step 1 are searched for medial axes and surfaces, which are detected based on the second-order approximation of $I(\mathbf{x}; \sigma_f)$. The medial axis and surface extraction is based on a formal analysis of the second-order 3-D local intensity structure. Here, σ_f is the filter scale used in medial axis/surface detection, and we assume that the width range of structures of interest is around the width at which the filter with σ_f gives the peak response (see [7] and [9] for detailed discussions).

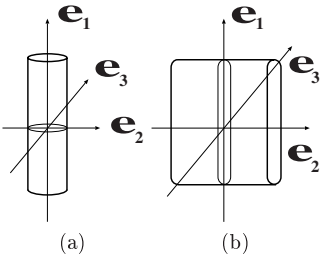

Fig. 1. Line and sheet models with the eigenvectors of the Hessian matrix. (a) Line. (b) Sheet.

Line Case – Medial Axis Detection – We assume that the tangential direction is given by $\mathbf{e}_1$ at the voxel around the medial axis. The 2-D intensity function, $C(\mathbf{u})$ ($\mathbf{u} = (u, v)^\top$), on the cross-sectional plane of $I(\mathbf{x}; \sigma_f)$ orthogonal to $\mathbf{e}_1$, should have its peak on the medial axis. The second-order approximation of $C(\mathbf{u})$ is given by

$$C(\mathbf{u}) = I(\mathbf{x}_0; \sigma_f) + \mathbf{u}^\top \nabla C_0 + \frac{1}{2}\mathbf{u}^\top \nabla^2 C_0 \mathbf{u}, \tag{3}$$

where $u\mathbf{e}_2 + v\mathbf{e}_3 = \mathbf{x} - \mathbf{x}_0$, $\nabla C_0 = (\nabla I \cdot \mathbf{e}_2, \nabla I \cdot \mathbf{e}_3)^\top$ (∇I is the gradient vector, that is, $\nabla I(\mathbf{x}_0; \sigma_f)$), and

$$\nabla^2 C_0 = \begin{bmatrix} \lambda_2 & 0 \\ 0 & \lambda_3 \end{bmatrix}. \tag{4}$$

$C(\mathbf{u})$ should have its peak on the medial axis of the line. The peak is located at the position satisfying

$$\frac{\partial}{\partial u} C(\mathbf{u}) = 0 \quad \text{and} \quad \frac{\partial}{\partial v} C(\mathbf{u}) = 0. \tag{5}$$

By solving Eq. (5), we have the offset vector, $\mathbf{p} = (p_x, p_y, p_z)^\top$, of the peak position from $\mathbf{x}_0$ given by

$$\mathbf{p} = s\mathbf{e}_2 + t\mathbf{e}_3, \tag{6}$$

where $s = -\frac{\nabla I \cdot \mathbf{e}_2}{\lambda_2}$ and $t = -\frac{\nabla I \cdot \mathbf{e}_3}{\lambda_3}$. For the medial axis to exist at the voxel $\mathbf{x}_0$, the peak of $C(\mathbf{u})$ needs to be located in the territory of voxel $\mathbf{x}_0$. Thus, the medial axis is detected only if $|p_x| \leq \frac{1}{2}$ & $|p_y| \leq \frac{1}{2}$ & $|p_z| \leq \frac{1}{2}$. By combining the voxel position $\mathbf{x}_0$ and offset vector $\mathbf{p}$, the medial axis is localized at subvoxel resolution.

Sheet Case – Medial Surface Detection – We assume that the direction of the surface normal is given by $\mathbf{e}_1$ at the voxel around the medial surface. The 1-D intensity function, $C(v)$, which is the profile of $I(\mathbf{x}; \sigma_f)$ along to $\mathbf{e}_3$, should

have its peak on the medial surface. The second-order approximation of $C(v)$ is given by

$$C(v) = I(\mathbf{x}_0; \sigma_f) + vC_0' + \frac{1}{2}v^2 C_0'', \tag{7}$$

where $v\mathbf{e}_3 = \mathbf{x} - \mathbf{x}_0$, $C_0' = \nabla I \cdot \mathbf{e}_3$, and $C_0'' = \lambda_3$. $C(v)$ should have its peak on the medial surface of the sheet. The peak is located at the position satisfying

$$\frac{d}{dv}C(v) = 0. \tag{8}$$

By solving Eq. (8), we have the offset vector, $\mathbf{p}$, of the peak position from $\mathbf{x}_0$ given by

$$\mathbf{p} = t\mathbf{e}_3, \tag{9}$$

where $t = -\frac{\nabla I \cdot \mathbf{e}_3}{\lambda_3}$. The medial surface is detected only if $|p_x| \leq \frac{1}{2}$ & $|p_y| \leq \frac{1}{2}$ & $|p_z| \leq \frac{1}{2}$.

Embedding Moving Frames The moving frame is defined by the voxel position $\mathbf{x}_0$, the offset vectors $\mathbf{p}$, and the eigenvectors $\mathbf{e}_1$, $\mathbf{e}_2$, $\mathbf{e}_3$ at each detected point of a medial axis or surface. In order to perform the subsequent processes based on moving frames, each voxel within the candidate regions obtained in Step 1 needs to be related to the moving frame. First, we find the correspondences between each voxel and one of the detected points of a medial axis or surface. Once these correspondences are found, each voxel is directly related to its corresponding moving frame. To find the correspondences, we use the Voronoi tessellation of the detected points. The territory of the detected point in the Voronoi tessellation can be regarded as the set of voxels to which each discrete moving frame is applied. This process is identical in both the line and sheet cases.

2.2 Subvoxel Edge Localization and Width Quantification

An adaptive directional second derivative is applied at each voxel based on its corresponding moving frame. The directional derivative is taken along the perpendicular from the voxel to the medial axis or surface. The zero-crossing points of the directional second derivatives are localized at subvoxel resolution to determine the precise region boundaries and quantitate the widths.

Line Case At every voxel within the candidate regions, the directional second derivative is calculated depending on its corresponding moving frame. The directional derivative is written as

$$D_{line}(\mathbf{x}; \sigma_e) = \mathbf{r}(\mathbf{x})^\top \nabla^2 I(\mathbf{x}; \sigma_e)\mathbf{r}(\mathbf{x}), \tag{10}$$

where $\mathbf{r}(\mathbf{x})$ is the unit vector whose direction is parallel to the perpendicular from the voxel position $\mathbf{x}$ to the straight line defined by the origin and the medial axis direction of the moving frame. The foot of the perpendicular can be regarded

as the corresponding axis position. The origin is given by the voxel position of the medial axis point and the offset vector $\mathbf{p}$. σ_e is the filter scale used in the edge localization; it is desirable that σ_e be small compared with the line width for accurate edge localization.

After the adaptive derivatives have been calculated at all the voxels, subvoxel edge localization is carried out at every voxel in the candidate regions. Let $\mathbf{o}_a$ be the foot of the perpendicular on the axis. Let $\mathbf{r}_a$ be the direction from $\mathbf{o}_a$ to the voxel position $\mathbf{x}_a$. For each voxel, we reconstruct the profiles originating from $\mathbf{o}_a$ in the directions $\mathbf{r}_a$ and $-\mathbf{r}_a$ for $D_{line}(\mathbf{x};\sigma_e)$ and the initial regions (which we specify as $B_{line}(\mathbf{x})$) obtained in Step 1. The edges are then localized in both directions and the width is calculated as the distance between the two edge locations. The profile is reconstructed at subvoxel resolution by using a trilinear interpolation for $D_{line}(\mathbf{x};\sigma_e)$ and a nearest-neighbor interpolation for $B_{line}(\mathbf{x})$.

Let $D_+(r)$ and $D_-(r)$ be the profiles of $D_{line}(\mathbf{x};\sigma_e)$ along the two opposite directions $\mathbf{r}_a$ and $-\mathbf{r}_a$ from $\mathbf{o}_a$. Let $B_+(r)$ and $B_-(r)$ be the profiles of $B_{line}(\mathbf{x})$. Here, r denotes the distance from the foot of the perpendicular on the axis. The localization of edges consists of two steps; finding the initial point for the subsequent search using $B_+(r)$, and then searching for the zero-crossing of $D_+(r)$. The initial point, p_0, is given by r of the first encountered point satisfying $B_+(r) = 0$, starting the search from $r = 0$, that is, the axis point. Given the initial point of the search, if $D_+(p_0) < 0$, search outbound from the axis point along the profile for the zero-crossing position r_+; otherwise, search inbound. After r_- has been similarly estimated, the width (diameter) is given by $|r_+ - r_-|$.

Sheet Case At every voxel within the candidate regions, the directional second derivative is taken orthogonal to both $\mathbf{e}_1$ and $\mathbf{e}_2$, that is, along $\mathbf{e}_3$, in its corresponding moving frame. The directional derivative is written as

$$D_{sheet}(\mathbf{x};\sigma_e) = \mathbf{s}(\mathbf{x})^\top \nabla^2 I(\mathbf{x};\sigma_e)\mathbf{s}(\mathbf{x}), \tag{11}$$

where $\mathbf{s}(\mathbf{x})$ is the unit vector whose direction is parallel to the medial surface normal of the moving frame. Using a method analogous to that employed in the line case, the profiles of $D_{sheet}(\mathbf{x};\sigma_e)$ and $B_{sheet}(\mathbf{x})$ are reconstructed for the directions $\mathbf{s}$ and $-\mathbf{s}$. These profiles are then used to determine the edge locations in the two directions and the width (thickness).

3 Experimental Results

3.1 Synthesized Images

We evaluated the medial axis detection performance and width estimation accuracy using synthesized 3-D images of lines and sheets with pill-box cross-sections and bar profiles, respectively. A simulated partial volume effect was incorporated when synthesizing the images. We focused on the effects of the filter scales σ_f

and σ_e, which are used in medial axis/surface detection and width quantification, respectively, on the detection and quantification of various widths of line and sheet structures.

Medial Axis Detection Synthesized 3-D images of a line with a circular axis were generated. The diameter of the line, D, was varied between 2.0 and $8\sqrt{2}(\simeq 11.3)$ pixels. The radius of the circular axis was proportional to D (we used $4 \times D$). Gaussian noise with 25 % standard deviation in the intensity height of pill-box cross-sections was added to the images. After line and sheet enhancement filtering with integration of scales appropriate for the line diameter [7],[9], the candidate regions were extracted by thresholding and extracting large connective components. The medial axis points were detected within these regions using the procedures described in Section 2.1 with two values for the filer scale σ_f, $\sqrt{2}$ ($\simeq 1.4$) and 4.0 pixels. The same candidate regions were used for both values of σ_f.

Figure 2 shows the volume rendering of the synthesized 3-D images and typical axis detection results. The detection was successful using appropriate combinations of line diameter D and filter scale σ_f (Fig. 2(b)). Many axis points are overlooked when the filter scale is larger than appropriate, while a number of false detections are made when the filter scale is smaller than appropriate (Fig. 2(c)).

Figure 3 shows the performance evaluation results. Detected axis points were evaluated by comparing them with analytically determined axis points. We regarded a detected point as a true detection if the distance between its position and one of the analytically determined points was within two pixels; otherwise, detected points were regarded as false. The false and true positive detection ratios are shown in Figs. 3(a) and (b); the plots verify the observations in Fig. 2. The positions and directions of the detected axis points regarded as true detections were compared with analytically determined ones (Figs. 3(c) and (d)). These graphs clarify the effect of σ_f on accurate and reliable axis detection.

Quantification Synthesized images of a line with a straight axis were generated with and without the same Gaussian noise as that used in the previous experiment. The line diameter D was again varied between 2.0 and $8\sqrt{2}(\simeq 11.3)$ pixels. Medial axis detection was carried out with the filter $\sigma_f = 2D$. The diameter estimation procedures described in Section 2.2 were applied using two values for the filter scale σ_e, $\sqrt{2}$ and 4.0 pixels. The results are shown in Fig 4 (a). Note that the diameter was underestimated when $\sigma_e < \frac{D}{\sqrt{2}}$, which is unlike the case of 2-D line diameter estimation [4], while it was overestimated when $\sigma_e > \frac{D}{2}$ and the error was quite small when $\sigma_e \ll \frac{D}{2}$, both of which are similar to the 2-D line case.

Synthesized images of a sheet with a spherical shape were used with and without Gaussian noise to determine the relationship between the estimated and true thickness. A similar relationship to that in the 2-D line case was observed (Fig 4 (b)).

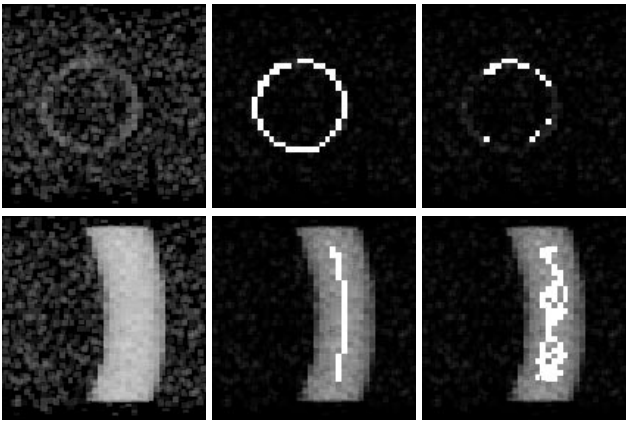

(a) (b) (c)

Fig. 2. Medial axis detection from synthesized 3-D images. All units are pixels. (a) Volume-rendered images of original synthesized 3-D images with Gaussian noise. Upper: $D = 2.0$. Lower: $D = 11.3$. (b) Examples of successful axis detection where the filter scale σ_f is appropriate for the line diameter D. The detected axis points are shown as bright points. Upper: $D = 2.0$, $\sigma_f = 1.4$. Lower: $D = 11.3$, $\sigma_f = 4.0$. (c) Examples of undesirable axis detection. Upper: $D = 2.0$, $\sigma_f = 4.0$. When diameter D is smaller than that appropriate for the filter scale σ_f, many true axis points are overlooked. Lower: $D = 11.3$, $\sigma_f = 1.4$. When D is larger than that appropriate for σ_f, many false axis points are detected.

3.2 Clinical Images

Diameter Estimation of Bronchial Airways from CT Images In this experiment, we used chest CT images taken by a helical CT scanner. The original voxel dimensions were $0.29 \times 0.29 \times 1.0$ (mm^3). In order to make the voxel isotropic, sinc interpolation was applied along the z-direction. The volume size used in the experiment was $90 \times 70 \times 80$ (voxels) after interpolation.

Fig. 5(a) shows the original CT images. After the initial region extraction by thresholding the line filtered images, the medial axis was detected using $\sigma_f = \sqrt{2}$, 2, and $2\sqrt{2}$ pixels. Fig. 5(b) shows the results of axis detection at the three different scales. Note that the axis points of thin structures were detected only at the smaller two scales while those of large structures (the right segment) were stably extracted at the larger two scales. Fig. 5(c) shows the results of diameter estimation using $\sigma_e = 1.2$ pixels based on the medial axes at these three scales.

Thickness Estimation of Hip Joint Cartilages from MR Images In this experiment, we used MR images of a hip joint with cartilage enhancement imaging [12]. The original voxel dimensions were $0.62 \times 0.62 \times 1.5$ (mm^3). Sinc interpolation was applied along the z-direction to make the voxel isotropic, and then

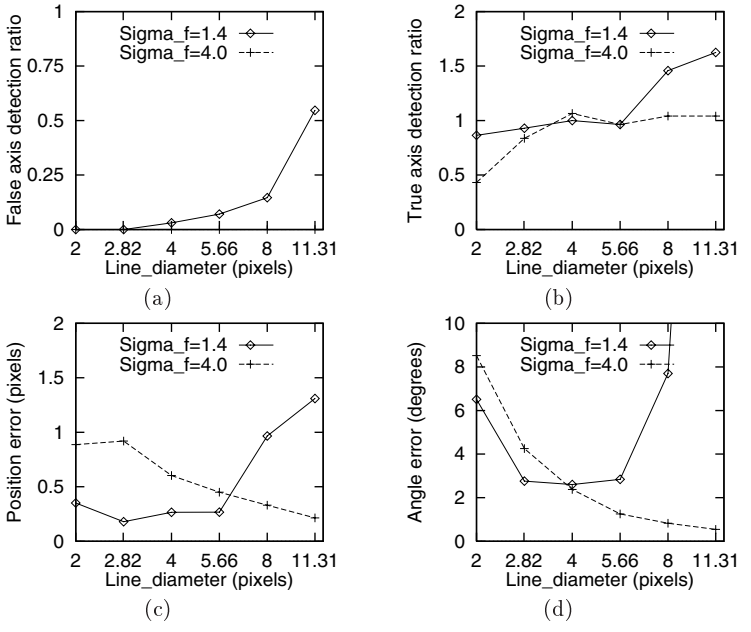

Fig. 3. Performance evaluation of medial axis detection. See text for the definitions of true and false detections. (a) False positive detection ratio, which is the ratio of the number of false detections to all the detections. The ratio was zero for all the line diameters at $\sigma_f = 4.0$ pixels. (b) True positive detection ratio, which is the ratio of the number of true detections to all the analytically determined points. (c) Average position error of axis points regarded as true detections. The distance between detected points and analytically determined points was used as the error. (d) Average angle error of the directions of axis points regarded as true detections.

further applied along all the three directions to make the resolution double. The resultant sampling pitch was 0.31 (mm) in all the three directions. The volume size used in the experiment was $256 \times 256 \times 100$ (voxels) after interpolation.

As shown in Fig. 6(a), cartilages are thin structures; thickness distributions are considered to be particularly important in the diagnosis of joint diseases. The initial cartilage regions were extracted from the enhanced images by the sheet filter. The medial surfaces were extracted using $\sigma_f = 1.4$ pixels. Figs. 6(b) and (c) show the results of thickness distribution estimated using $\sigma_e = 1.2$ pixels. We also obtained the thickness distributions using $\sigma_e = 1.0$ pixel for comparison purposes. The average thickness estimated using $\sigma_e = 1.2$ pixels was $T_f = 4.24$ pixels and $T_a = 3.50$ pixels for the femoral and acetabular cartilages, respectively, compared with $T_f = 4.16$ pixels and $T_a = 3.39$ pixels using $\sigma_e = 1.0$ pixel.

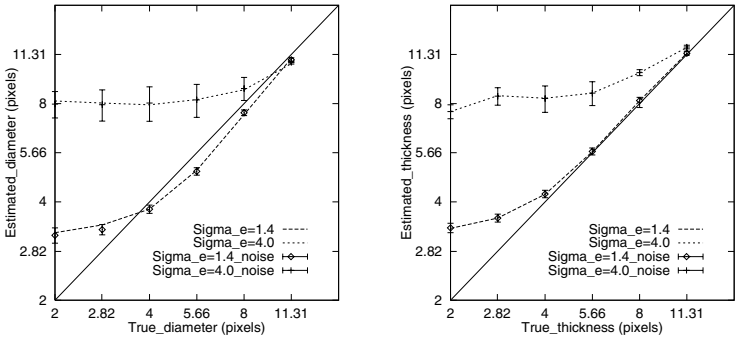

Fig. 4. Accuracy of quantification. The results for the images with 25 % noise are shown by dotted lines. Error bars indicate the standard deviation in the estimated diameters. (a) Diameter estimation of line with a straight axis. (b) Thickness estimation of sheet with a spherical shape.

In previous work [13], hip joint cartilages were assumed to be distributed on a sphere approximating the femoral head. The user needs to specify the center of the sphere, and the cartilage thickness is then estimated along radial directions from the specified center. The method proposed here does not use the sphere assumption, and thus can potentially be applied to badly deformed hip joints as well as to articular cartilages of other joints.

4 Conclusions

The novel method proposed in this paper for detecting and quantitating 3-D line and sheet structures has the following advantages: (1) Well-defined medial axes and surfaces are automatically detected and localized with subvoxel accuracy. (2) The direction along which the width is measured can be automatically estimated. (3) Subvoxel accuracy in width quantification is attainable. These advantages are obtained because the method was formulated based on a thorough analysis of second-order 3-D local intensity structures as a continuous 3-D function. The accuracy limits and the effects of the filter scales on the detection and quantification accuracy were evaluated using synthesized images with various line and sheet structure widths. Finally, the experiments using 3-D CT and MR images demonstrated the applicability of the method to clinical problems.

Future work will address the following issues. Firstly, the behavior of the method at bifurcation and tangency should be examined. Secondly, a method for multiscale integration needs to be developed to combine medial axes and surfaces detected at different scales. Thirdly, the proposed method assumes the isotropy of voxels in 3-D images. However, medical 3-D data generally have lower resolution along the third direction (the direction orthogonal to the slice

plane) than within slices, which means that the voxels are essentially anisotropic. Hence, the effects of anisotropic voxels on accuracy requires investigation. Finally, clinical validation using a large set of data for each specific application is an important aspect of future work.

Acknowledgment This work was partly supported by the Japan Society for the Promotion of Science (JSPS Research for the Future Program and JSPS Grant-in-Aid for Scientific Research (C)(2) 11680389). This work was conducted in collaboration with the Department of Radiology and the Department of Orthopaedic Surgery, Osaka University Graduate School of Medicine.

References

1. B.G. Brown, E.L. Bolson, M. Frimer, *et al.*: Quantitative coronary arteriography, *Circulation*, **55**, 329-337, (1977).
2. J.H.C. Reiber, C.J. Kooijman, C.J. Slager, *et al.*: Coronary artery dimensions from cineangiograms — methodology and validation of a computer-assisted analysis procedure, *IEEE Transactions on Medical Imaging*, **3**(3), 131-141 (1984).
3. Y. Sato, T. Araki, M. Hanayama, *et al.*: A viewpoint determination system for stenosis diagnosis and quantification in coronary angiographic image acquisition, *IEEE Transactions on Medical Imaging*, **17**(1), 121–137 (1998).
4. C. Steger: An unbiased detector of curvilinear structures: *IEEE Transactions on Pattern Analysis and Machine Intelligence*, **20**(2), 113-125 (1998).
5. T.M. Koller, G. Gerig, G. Szekely, *et al.*: Multiscale detection of curvilinear structures in 2-D and 3-D image data, *Proc. Fifth International Conference on Computer Vision* (*ICCV'95*), Boston, MA, 864-869 (1995).
6. B.S. Morse, S.M. Pizer, and A. Liu: Multiscale medical analysis of medical images: *Image and Vision Computing*, **12**(6): 327–338 (1994).
7. Y. Sato, S. Nakajima, N. Shiraga, *et al.*: Three dimensional multi-scale line filter for segmentation and visualization of curvilinear structures in medical images, *Medical Image Analysis*, **2**(2), 143–168 (1998).
8. K. Krissian, G. Malandain, N. Ayache, *et al.*: Model-based multiscale detection of 3D vessels, *Proc. IEEE Conference on Computer Vision and Pattern Recognition* (*CVPR'98*), Santa Barbara, CA, (1998).
9. Y. Sato, C-F Westin, A. Bhalerao, *et al.*: Tissue classification based on 3D local intensity structures for volume rendering, *IEEE Transactions on Visualization and Computer Graphics*, **6**(2), 160-180 (2000).
10. T. O'Donnell, A. Gupta, and T. Boult: A new model for the recovery of cylindrical structures from medical image data, *Lecture Notes in Computer Science* (*LNCS*), **1205** (*CVRMed-MRCAS'97*), 223-232 (1997).
11. A.F. Frangi, W.J. Niessen, R.M. Hoogeveen, *et al.*: Model-based quantification of 3-D magnetic resonance angiographic images, *IEEE Transactions on Medical Imaging*, **18**(10), 946-956, (1999)
12. N. Nakanishi, H. Tanaka, T. Nishii, *et al.*: MR evaluation of the articular cartilage of the femoral head during traction, *Acta Radiologica*, **40**, 60-63 (1999).
13. Y. Sato, T. Kubota, K. Nakanishi, *et al.*: Three-dimensional reconstruction and quantification of hip joint cartilages from magnetic resonance images, *Lecture Notes in Computer Science* (*LNCS*), **1679** (*MICCAI'99*), 338–347 (1999).

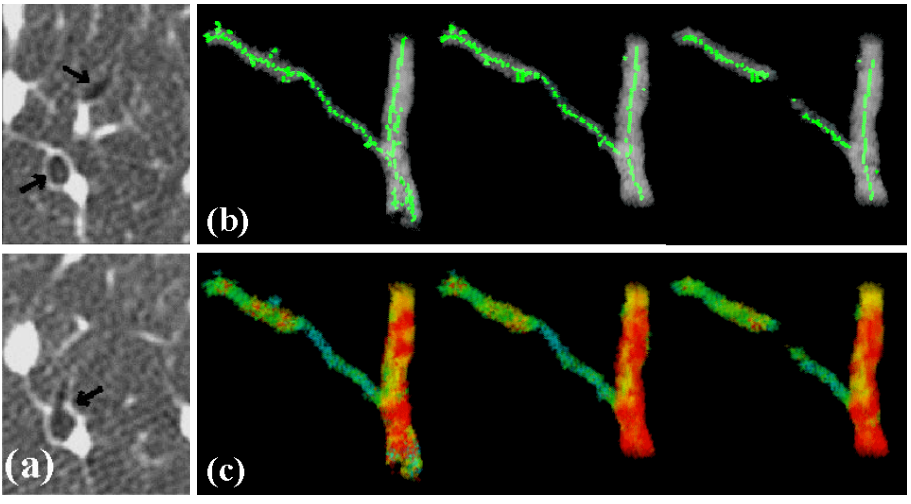

Fig. 5. Diameter estimation of bronchial airways from CT images. (a) Original CT images. The bronchial airway regions, which are darker than the surrounding structures, are shown by arrows. (b) Detection of medial axes at three different scales. Left: $\sigma_f = 1.4$ pixels. Middle: $\sigma_f = 2.0$ pixels. Right: $\sigma_f = 2.8$ pixels. (c) Diameter estimation at the three different scales. The estimated diameter is coded by color: red and blue represent large and small diameters, respectively.

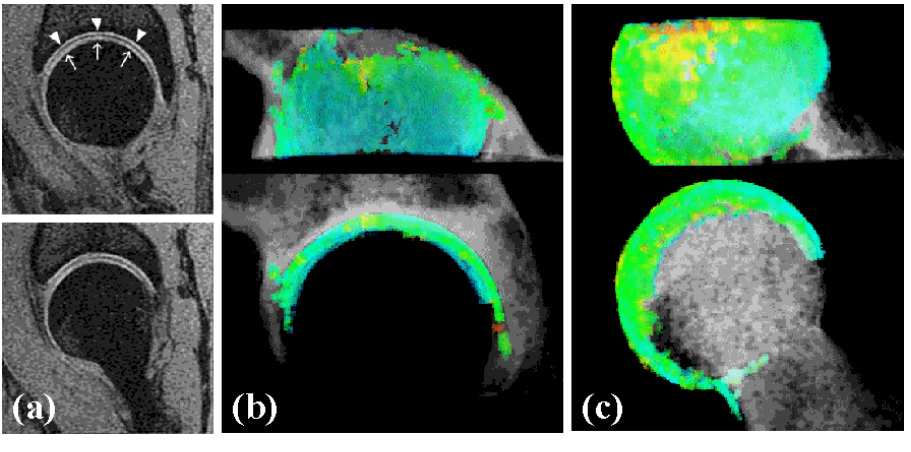

Fig. 6. Thickness estimation of cartilages from MR images. (a) Original MR images. The acetabular (pelvic side) cartilages are shown by arrowheads, and the femoral head cartilages by arrows. (b) Thickness distribution of acetabular cartilages. The estimated thickness is coded by color in the same way as in Fig. 5. The bone regions are volume-rendered in white. (c) Thickness distribution of femoral cartilages.